RSC Advances

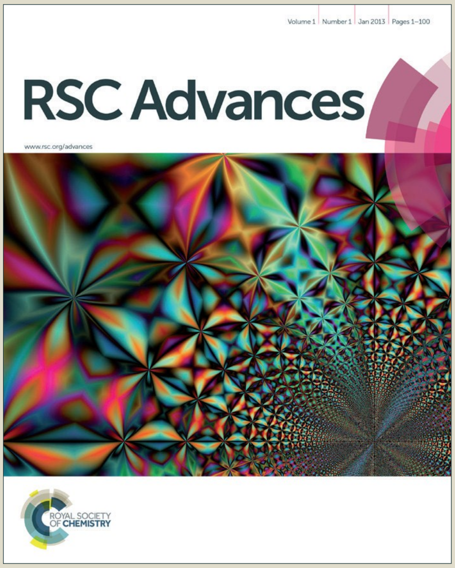

ROYAL SOCIETY OF CHEMISTRY

www.rsc.org/advances

Journal Name

ARTICLE

Received 00th January 20xx,
Accepted 00th January 20xx

DOI: 10.1039/x0xx00000x

www.rsc.org/

Preparation of Pd_xAu_y bimetallic nanostructures with controllable morphologies supported on reduced graphene oxide nanosheets and wrapped in polypyrrole layer

Tongjie Yao,[a,b] Quan Zuo,[a] Hao Wang,[a] Jie Wu,[c] Xiao Zhang,[a,b] Jianmin Sun[*a,b] and Tieyu Cui[*b]

In this paper, we have introduced a one-step method to prepare Pd_xAu_y bimetallic nanostructures supported on reduced graphene oxide (rGO) nanosheets and wrapped in polypyrrole (PPy) layer. By using pyrrole monomer as special reducing agent for metal salt, the morphologies of Pd_xAu_y bimetallic nanostructures could be easily turned to be spherical, coral-like and porous cluster-like *via* simply changing dosage or molar ratio of $PdCl_2$ and $HAuCl_4·4H_2O$. The roles of pyrrole monomer and rGO support in formation of rGO/Pd_xAu_y/PPy composites were investigated in detail. Transmission electron microscopy, elemental mapping analysis, X-ray diffraction, X-ray photoelectron spectroscopy and Fourier-transform infrared spectra were used to character their morphologies, structures and compositions. Compared with corresponding rGO/Pd/PPy and rGO/Au/PPy composites, the as-prepared rGO/Pd_xAu_y/PPy composites displayed enhanced catalytic activity towards the reduction of 4-nitrophenol.

Introduction

Owing to fantastic physical, chemical and biological properties, metal nanoparticles are widely applied in surface enhanced spectroscopy, biological imaging, optoelectronic, sensor and especially in catalysis.[1,2] Numerous studies indicate metal nanoparticles exhibit high catalytic activities toward different types of reactions, including reduction of dyes, Heck C-C coupling and hydrogenation reaction.[3] Compared with monometallic nanoparticles, the bimetallic nanoparticles often display enhanced catalytic activity and selectivity due to their special ensemble and ligand effects;[4] therefore, more and more attentions have been paid to bimetallic catalysts made of two or more components. However, similar to monometallic nanoparticles, a major obstacle for practical use of the bimetallic nanoparticles as catalysts is their tendency to aggregation under real reaction conditions. These nanoparticles are usually subject to sintering or coalescence to minimize their surface energies, thus losing catalytic activity.[5] It has been confirmed through investigation that loading nanoparticles on an appropriate support is an effective way to overcome the above drawback.[6,7]

For catalysts support, it is usually required to provide high surface area, good stability, robust surface chemistry and excellent dispersion characteristic, which is important for optimizing the synergistic nanoparticle-support interaction and maximizing the reactive activity of metal catalysts. Based on the principle, graphene nanosheets are ideal candidates due to their high surface area, mechanical strength and conductivity. Many groups have combined the bimetallic nanoparticles and reduced graphene oxide (rGO) nanosheet together to further improve catalytic activity, and the most commonly used procedure is reduction of the mixture of graphene oxide (GO) nanosheets and bimetallic salt by chemical or thermal method.[8-12] The approach is simple; however, the as-prepared bimetallic nanoparticles on rGO nanosheet surface usually only exhibit spherical morphology. It is well known the catalytic reactions take place on the nanostructure surface, slight changes in the sizes, structures, compositions or morphologies can influence catalytic activity. Therefore, the development of bimetallic nanostructures with non-spherical morphologies, especially the controllable morphologies, is of great importance.

In the past two decades, conducting polymers have stimulated increasing interest owing to their good conductivity, redox property, stability and biocompatibility.[13,14] The applications of conducting polymer in the field of catalysis have also aroused considerable attentions. On one hand, the coordination interaction generated between functional groups on their backbone and metal salt can effectively hinder the aggregation of metal nanoparticles;[15] on the other hand, their good conductivity is beneficial for transformation of electron in the catalytic reaction.[16] Moreover, conducting polymer monomer can be used as reducing agent for metal salt, which leads to synthesis of conducting polymer and metal nanoparticles in one-step.[17-19] Based on the aforementioned statements, herein, we selected pyrrole monomer as a special reducing agent to prepare rGO/Pd_xAu_y/polypyrrole (PPy)

---

[a] State Key Laboratory of Urban Water Resource and Environment, Harbin Institute of Technology, Harbin 150090, China; E-mail: sunjm@hit.edu.cn.
[b] The Academy of Fundamental and Interdisciplinary Science, Harbin Institute of Technology, Harbin 150080, China; E-mail: cuit@hit.edu.cn
[c] Key Laboratory of Functional Inorganic Material Chemistry, Ministry of Education, School of Chemistry and Materials Science, Heilongjiang University, Harbin 150080, China

Electronic Supplementary Information (ESI) available: [details of any supplementary information available should be included here]. See DOI: 10.1039/x0xx00000x composites with Pd_xAu_y bimetallic nanostructure supported on rGO nanosheets and wrapped in PPy layer. With the help of both pyrrole monomer and rGO support, the resulting bimetallic nanostructures not only exhibited high dispersity, but also had good stability. Importantly, their morphologies could be easily turned to be spherical, coral-like and porous cluster-like *via* simply changing the molar ratio or dosage of $PdCl_2$ and $HAuCl_4{\cdot}4H_2O$. The catalytic property of rGO/Pd_xAu_y/PPy composites was investigated by reducing the 4-nitrophenol (4-NP) with $NaBH_4$ as the reducing agent. Compared with monometallic composites, such as rGO/Pd/PPy and rGO/Au/PPy composites, they showed higher catalytic activity.

Experimental method

Materials

The pyrrole monomer was purchased from Sigma-Aldrich, and it was distilled under reduced pressure and stored at -4 ^oC prior to use. $PdCl_2$, $HAuCl_4{\cdot}4H_2O$, $NaBH_4$, KNO_3, $KMnO_4$, H_2SO_4, H_2O_2 (30 wt%), graphite, and 4-NP were purchased from Sinopharm Chemical Reagent Co., Ltd. All of chemicals were analytical grade and used as received. The water used in the experiments was deionized with a resistivity of 18.2 $M\Omega{\cdot}cm^{-1}$.

Preparation of rGO/Pd_xAu_y/PPy composites

GO nanosheets were prepared by Hummer's method and the concentration was adjusted to 1.7 mg/mL.[20] Typically, 5.0 mL aqueous solution of $PdCl_2$ (1.05×10^{-5} mol) and $HAuCl_4{\cdot}4H_2O$ (1.05×10^{-5} mol) was added into 20 mL GO solution. After magnetic stirring for 30 min, 10 mL pyrrole monomer solution (0.5 wt%) was added into above mixture. The redox reaction was allowed to proceed for 6.0 h. Finally, the products were centrifuged and washed by deionized water for 3 times. After investigating the molar ratio of elemental Pd to Au in composites by inductively coupled plasma atomic spectrum (ICP), the as-prepared sample was denoted as rGO/$Pd_{48}Au_{52}$/PPy composites.

For comparison purposes, other catalysts were prepared by the same procedure, except some parameters were slightly changed. To prepare rGO/Au/PPy, rGO/$Pd_{34}Au_{66}$/PPy, rGO/$Pd_{75}Au_{25}$/PPy and rGO/Pd/PPy composites, the total dosage of $PdCl_2$ and $HAuCl_4{\cdot}4H_2O$ was fixed at 2.1×10^{-5} mol, while their molar ratio was changed to be 0:4, 1:3, 3:1 and 4:0, respectively. To prepare rGO/$(Pd_{48}Au_{52})_{0.5}$/PPy, rGO/$(Pd_{48}Au_{52})_2$/PPy and rGO/$(Pd_{48}Au_{52})_4$/PPy composites, the molar ratio of $PdCl_2$ to $HAuCl_4{\cdot}4H_2O$ was fixed at 1:1, while the total dosage of $PdCl_2$ and $HAuCl_4{\cdot}4H_2O$ was changed to be 1.05×10^{-5}, 4.2×10^{-5} and 8.4×10^{-5} mol, respectively. Two reference samples PdAu/PPy and rGO/PdAu composites were prepared *via* above approach except GO nanosheets were not used or pyrrole monomer was replaced by $NaBH_4$ solution (10 mL, 10 mM).

Catalyzed reduction of 4-NP

The catalytic property of rGO/Pd_xAu_y/PPy composites was explored by studying the change of the absorbance intensity at the maximum absorbance wavelength of the 4-NP. In a typical procedure, 0.2 mg rGO/Pd_xAu_y/PPy composites were homogeneously dispersed into the 2.9 mL 4-NP solution (18 mg L^{-1}), followed by a rapid injection of 0.1 mL of $NaBH_4$ solution (10 mg mL^{-1}) under stirring. The color of the mixture gradually changed from bright-yellow to colorless, indicating that the rGO/Pd_xAu_y/PPy composites catalyzed the reduction of 4-NP.

Characterization

A SU-8010 scanning electron microscopy (SEM) was employed to examine the surface morphologies of products. The structures of the catalysts were characterized by transmission electron microscopy (TEM), high resolution TEM (HRTEM) and high-angle annular dark-field scanning TEM (HAADF-STEM) on a Tecnai G^2 F30 transmission electron microscopy operating at an acceleration voltage of 300 KV. X-ray photoelectron spectroscopy (XPS) measurements were carried out on a VG ESCALAB MKII spectrometer with Mg Kα excitation (1253.6 eV). The UV-Visible (UV-Vis) absorption spectra in the wavelength range of 250~550 nm were obtained from a Lambda 750 spectrophotometer. Powder X-ray diffraction (XRD) measurements were carried out on a Siemens D-5005 apparatus, using the Cu Kα radiation (λ = 1.5418 Å). Fourier-transform infrared (FT-IR) spectra were measured over the wavenumber ranging from 400 to 4000 cm^{-1} using a Nicolet Avatar 360 FT-IR spectrophotometer. ICP measurement was performed on Optima 7000 DV.

Results and discussion

The synthetic scheme of rGO/Pd_xAu_y/PPy composites is shown in Fig. 1, which begins with preparation of GO nanosheets. After addition of pyrrole monomer into the mixture of GO nanosheets, $PdCl_2$ and $HAuCl_4{\cdot}4H_2O$ solution, the redox reaction immediately took place, since the solution color quickly turned from original brown (the color of GO solution) to black (the color of PPy). On one hand, GO nanosheets were reduced to rGO nanosheets;[21,22] while $PdCl_2$ and $HAuCl_4{\cdot}4H_2O$ were reduced to Pd_xAu_y bimetallic nanostructures. On the other hand, the as-prepared PPy layer not only covered on Pd_xAu_y bimetallic nanostructures to prevent their aggregation; but also coated on the rGO nanosheet surface, as positively charged PPy chains would nucleate on their surface *via* electrostatic force and π-π^* interactions.[23] Therefore, the rGO/Pd_xAu_y/PPy composites with Pd_xAu_y bimetallic nanostructures supported on the rGO nanosheets and wrapped in PPy layer were successfully prepared.

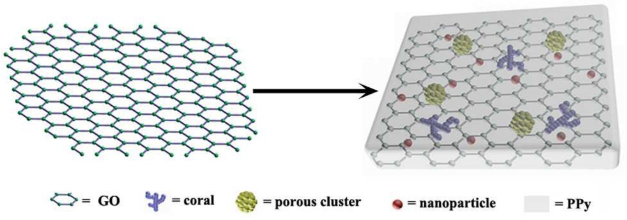

Fig. 1 Scheme for the synthesis of rGO/Pd_xAu_y/PPy composites.

Fig. 2 exhibits the representative TEM images of rGO/$Pd_{48}Au_{52}$/PPy composites at different magnifications. In low magnifications (Fig. 2a and 2b), $Pd_{48}Au_{52}$ bimetallic nanostructures uniformly disperse on the scrolled rGO nanosheet surface without aggregations in large area. No nanostructures outside of nanosheets can be found. The above phenomenon implied: first, a good combination existed between the rGO support and $Pd_{48}Au_{52}$ nanostructures; second, the coverage of PPy layer effectively prevented nanostructures from aggregations and falling off. In high magnifications (Fig. 2c and 2d), the $Pd_{48}Au_{52}$ nanostructures can be seen more clearly. Every nanostructure comprises of several spherical nanoparticles with diameter of about 4.5 nm, which makes them have many branches and look like "coral". When the molar ratio of $PdCl_2$ to $HAuCl_4 \cdot 4H_2O$ is 1:1, "coral-like" nanostructures occupy the most of TEM image view; however, some single nanoparticles still can be found, and their size is nearly the same as the nanoparticles that constitute the "coral", further suggesting "coral-like" nanostructures originate from assembly of nanoparticles.

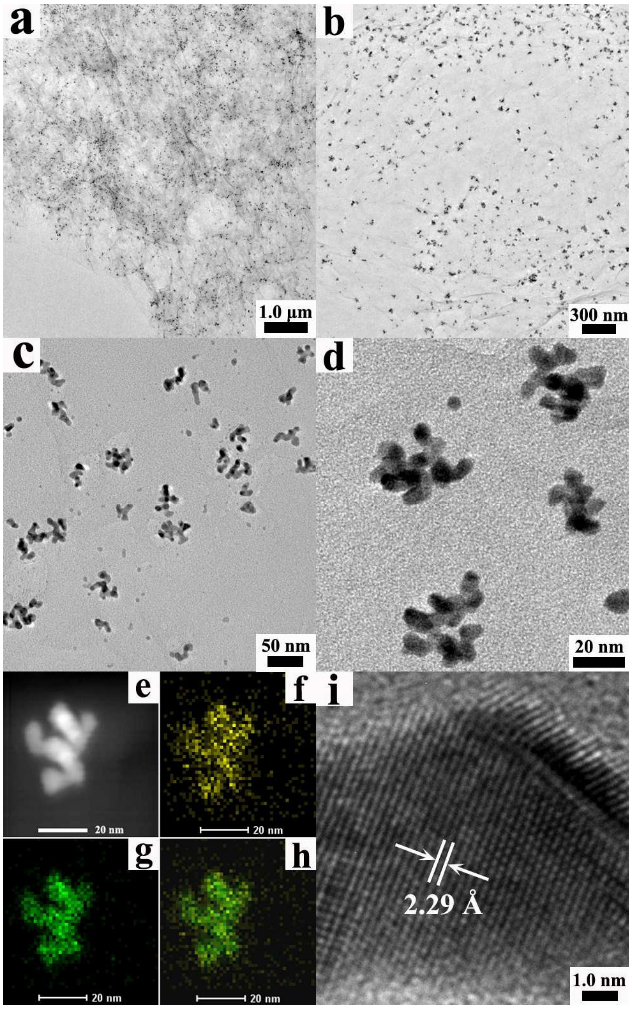

Fig. 2 (a-d) TEM images of rGO/$Pd_{48}Au_{52}$/PPy composites at different magnifications; (e) HAADF-STEM image of rGO/$Pd_{48}Au_{52}$/PPy composites; (f-h) elemental mapping of Au, Pd and Au&Pd; (i) HRTEM image of rGO/$Pd_{48}Au_{52}$/PPy composites.

To determine the distributions of element Pd and Au in "coral-like" nanostructures, HAADF-STEM measurements and corresponding elemental mapping analysis were carried out. Fig. 2e and 2f clearly show both Pd and Au have homogeneous distributions in "coral-like" nanostructure, and their distributions almost overlap with each other (Fig. 2h), suggesting the formation of $Pd_{48}Au_{52}$ alloy, rather than individual Pd or Au nanoparticles.[24-25] The alloy structure could be further confirmed through HRTEM image and XRD patterns. Fig. 2i reveals good crystallization of the $Pd_{48}Au_{52}$ nanostructures with a (111) lattice spacing of 2.29 Å, which is between the (111) lattice spacing of face centered cubic Pd (2.25 Å) and Au (2.36 Å) nanoparticles.[26] The XRD patterns of the rGO/Au/PPy, rGO/Pd/PPy and rGO/$Pd_{48}Au_{52}$/PPy composites are shown in Fig. 3. For rGO/Au/PPy composites (Fig. 3a), the peaks located at 38.16 , 44.3 and 64.69° are corresponding to of (111), (200) and (220) lattice planes of the Au nanoparticles (JCPDS No. 04-0784). For rGO/Pd/PPy composites (Fig. 3c), the peaks at 40.14 , 46.33 and 68.50° are assigned to the (111), (200) and (220) lattice planes of the Pd nanoparticles (JCPDS No. 05-0681). The XRD pattern of the rGO/$Pd_{48}Au_{52}$/PPy composites is presented in Fig. 3b, The peaks of $Pd_{48}Au_{52}$ nanostructures are located between the diffraction peaks of Au and Pd nanoparticles, indicating that Pd is incorporated into the face centered cubic Au structure to form an alloy phase with a concomitant lattice contraction.[27]

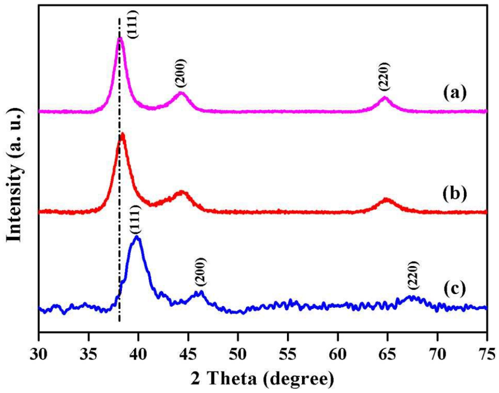

Fig. 3 XRD patterns of (a) rGO/Au/PPy composites; (b) rGO/$Pd_{48}Au_{52}$/PPy composites; (c) rGO/Pd/PPy composites.

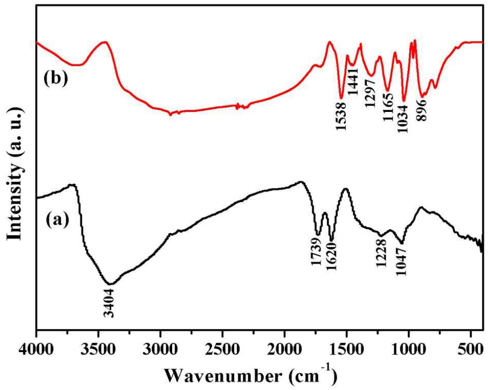

Fig. 4 FT-IR spectra of (a) original GO nanosheets; (b) rGO/$Pd_{48}Au_{52}$/PPy composites.

Fig. 4a shows the FT-IR spectra of GO nanosheets, their characteristic absorption peaks emerge at 3404, 1739, 1620, 1228 and 1047 cm^{-1}, which is in a good agreement with previous study.[28] After redox reaction, rGO/$Pd_{48}Au_{52}$/PPy composites were prepared and their FT-IR spectrum is shown in Fig. 4b. As PPy is a strong absorber in infrared region, the feature peaks belonged to rGO nanosheets are covered. The PPy characteristic peaks can be distinguished clearly: the bands at 1538 and 1441 cm^{-1} are attributed to the stretching mode of the C-C and C-N in the pyrrole ring. The peaks at 1297 and 1165 cm^{-1} are related to the in-plane vibrations of C-H. Besides these, ring deformation at 896 cm^{-1} is also observed.[29] Obviously, FT-IR spectrum reveals PPy is one of components in rGO/$Pd_{48}Au_{52}$/PPy composites. Further evidences of PPy existence and its distribution were provided by elemental mapping analysis. As shown in Fig. S1, the element N uniformly disperses on the rGO nanosheet surface, implying PPy layer covers on the whole rGO nanosheets.

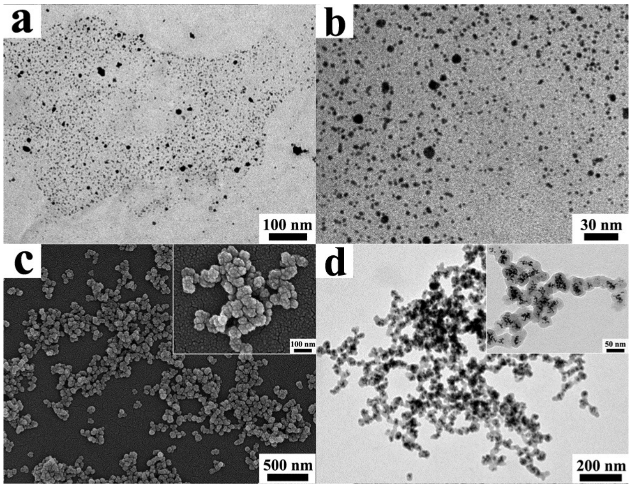

Fig. 5 (a, b) TEM and magnified TEM images of rGO/PdAu composites; (c, d) SEM and TEM images of PdAu/PPy composites, insets show the corresponding magnified images.

To reveal the reduction of GO nanosheets to rGO nanosheets during the redox reaction, the XPS measurements were carried out. Fig. S2a shows the survey XPS spectra of GO nanosheets before and after redox reaction. The spectrum of original GO nanosheets displays two major components at 282 and 529 eV corresponding to the signals of C 1s and O 1s, respectively. In spectrum of rGO/$Pd_{48}Au_{52}$/PPy composites, besides C 1s and O 1s signals, three new peaks located at 400, 337 and 85 eV are assigned to Pd 3d, N 1s and Au 4f, respectively. In Fig. S2b, the carbon species in original GO nanosheets are divided into four peaks: C-C/C=C (284.5 eV), C-O (286.5 eV), C=O (287.2 eV) and O-C=O (288.5 eV).[30] In rGO/$Pd_{48}Au_{52}$/PPy composites (Fig. S2c), they can be fitted into five peaks, as an additional C-N (285.6 eV) peak originated from PPy layer appears.[31] Compared with GO nanosheets, the content of oxidized carbon species decreases from original 64% to 45%, suggesting oxygen containing groups are reduced by pyrrole monomer. Based on the TEM images, XRD patterns, XPS and FT-IR spectra, we could conclude that rGO/Pd_xAu_y/PPy composites had been successfully prepared.

In previous study, the bimetallic nanostructures deposited on the rGO support *via* chemical or thermal reduction usually only exhibited spherical morphology.[9,10,26,27] Seldom paper reported non-spherical nanostructures on rGO nanosheet surface.[32,33] In our study, the "coral-like" $Pd_{48}Au_{52}$ alloy appeared on the rGO nanosheet surface by using pyrrole monomer as reducing agent. It was necessary to reveal the role of pyrrole monomer in formation of "coral-like" nanostructure. Fig. 5a and 5b show the TEM images of rGO/PdAu composites prepared by using $NaBH_4$ instead of pyrrole monomer. Similar to previous report,[9,10] only spherical nanoparticles can be observed on rGO nanosheet surface. Although most of nanoparticles are uniform with an average diameter of 4.0 nm, the large aggregations still can be seen. Additionally, some nanoparticles appear outside of rGO nanosheets. These results suggested that the pyrrole monomer helped to control the dispersity of the nanostructures and the formation of the "coral-like" geometry. Besides pyrrole monomer, the influence of rGO nanosheets in formation of rGO/$Pd_{48}Au_{52}$/PPy composites was also investigated. Fig. 5c and 5d show the SEM and TEM images of PdAu/PPy composites prepared in absence of rGO nanosheets. Only core/shell spherical composites with rough surface and diameter of tens of nanometers can be obtained. Their aggregations are very severe. When metal salts were reduced to the metal nanoparticles, owing to high surface energy, PPy chains immediately coated on their surface. Because of the strong hydrogen bond and π-π^* interactions between the PPy chains, severe aggregations inevitably took place.[34] The phenomenon indicated rGO nanosheets played important roles in uniformly dispersing both Pd_xAu_y nanostructures and PPy layer.

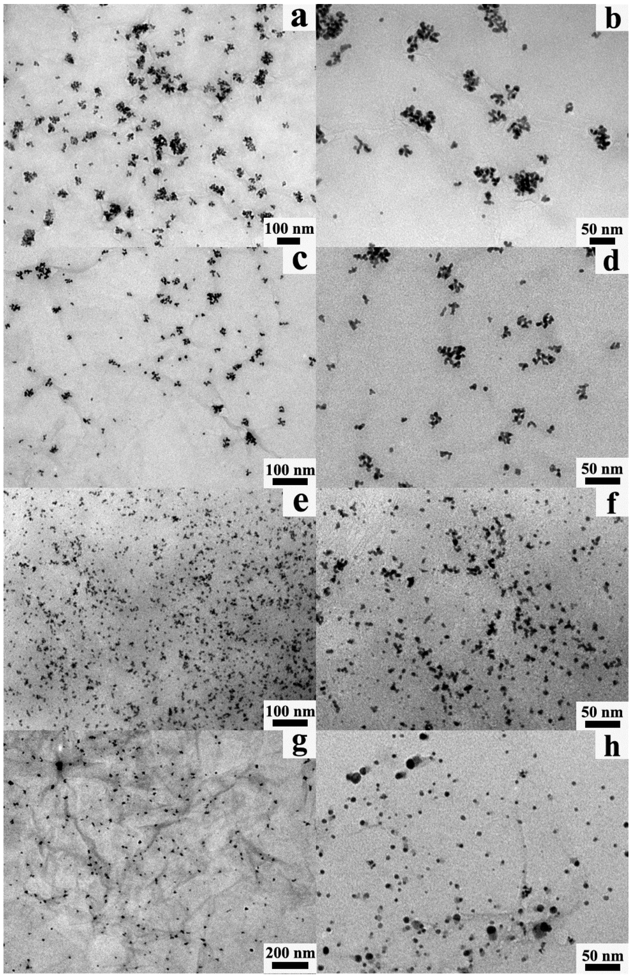

Fig. 6 TEM images of (a, b) rGO/Au/PPy composites; (c, d) rGO/$Pd_{34}Au_{66}$/PPy composites; (e, f) rGO/$Pd_{75}Au_{25}$/PPy composites; (g, h) rGO/Pd/PPy composites.

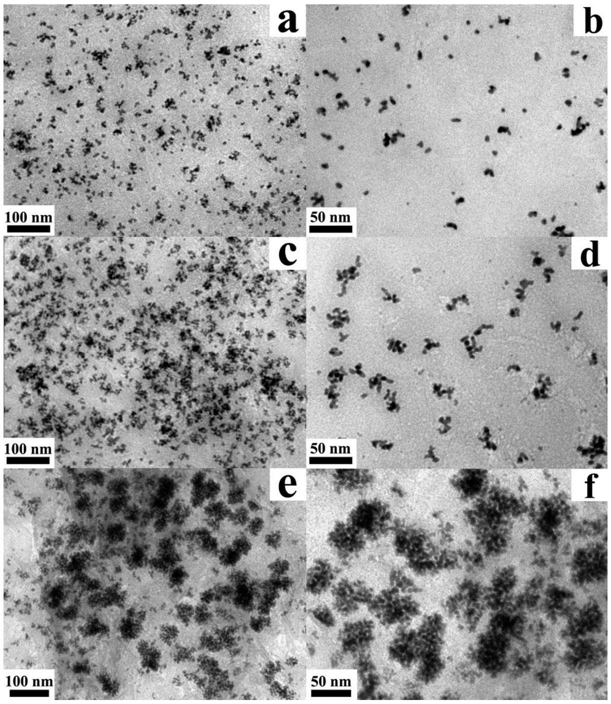

Fig. 7 TEM images of (a, b) rGO/$(Pd_{48}Au_{52})_{0.5}$/PPy; (c, d) rGO/$(Pd_{48}Au_{52})_2$/PPy; (e, f) rGO/$(Pd_{48}Au_{52})_4$/PPy composites.

The morphologies of Pd_xAu_y nanostructures could be easily adjusted *via* simply varying molar ratio of $PdCl_2$ to $HAuCl_4$. Fig. 6 shows the TEM images of Pd_xAu_y nanostructures prepared with different molar ratio of $PdCl_2$ to $HAuCl_4·4H_2O$. Without $PdCl_2$ (Fig. 6a and Fig. 6b), although few single Au nanoparticles can be observed, most of Au nanostructures appear as the "coral". With the ratio of $PdCl_2$ to $HAuCl_4·4H_2O$ increasing from 1:3 to 3:1 (Fig. 6c~6f and Fig. 2a~2d), the amount of "coral-like" nanostructures gradually decreases; while more and more single nanoparticles appear in the TEM image. For rGO/Pd/PPy composites (Fig. 6g and 6h), $PdCl_2$ tends to form Pd nanoparticles in absence of $HAuCl_4·4H_2O$. In addition to the molar ratio of $PdCl_2$ to $HAuCl_4·4H_2O$, the dosage of metal salt also had influence on morphologies of bimetallic nanostructures. Compared with Fig. 2, when the amount of metal salt decreases by half (Fig. 7a and 7b), the number of spherical nanoparticles dramatically increases. When the usage of metal salt is doubled (Fig. 7c and 7d), the number of "coral-like" nanostructures obviously increases, and it is hard to find single nanoparticles in the view of TEM image. When the dosage of metal salt is four times larger than that of Fig. 2 (Fig. 7e and 7f), the alloys assemble to the porous clusters with diameter of about 70 nm. It is necessary to mention that no aggregations occurs in these nanostructures with the help of rGO nanosheets and PPy layer. According to aforementioned study, we could conclude that the morphologies of Pd_xAu_y bimetallic nanostructures were easily turned from spherical to coral-like and to porous cluster-like *via* simply adjusting both molar ratio and usage of $PdCl_2$ and $HAuCl_4·4H_2O$.

As commonly known, the 4-NP was organic pollutant in industrial and agricultural waste water, whereas 4-aminophenol (4-AP) had a numerous applications including those in analgesic and antipyretic drugs and photographic developers.[35,36] It was of great significance that 4-NP could be efficiently reduced to 4-AP. Therefore, reduction of 4-NP to 4-AP was selected as a probe reaction to evaluate the catalytic activity of rGO/Pd_xAu_y/PPy composites. Typically, this reduction reaction could be catalyzed by metal catalysts at room temperature. The catalytic activity depended on the electron transformation from the BH_4^- donor to the acceptor 4-NP and the diffusion and adsorption of 4-NP on the catalyst surface. The reduction process of 4-NP was monitored by measuring the UV-Vis absorption spectra of the reaction solutions. Fig. 8a shows the spectrum of original 4-NP solution, a strong absorption peak emerges at 317 nm (curve a). After the addition of $NaBH_4$ into aqueous 4-NP solution, the color quickly turns from light-yellow to bright-yellow. The wavelength of absorption peak shifts from 317 to 400 nm due to the formation of 4-nitrophenolate anions under alkaline condition. Without catalysts, this reaction proceeds very slowly, even after reaction for 20 h, the intensity of peak at 400 nm only reduces 6.1% (curve c). In contrast, if 0.2 mg rGO/$Pd_{48}Au_{52}$/PPy catalysts are added into the reaction system, the peak at 400 nm quickly vanishes within 3.0 min, and a new peak emerged at 300 nm is attributed to the 4-AP (curve d), indicating the rGO/$Pd_{48}Au_{52}$/PPy composites have good catalytic property.

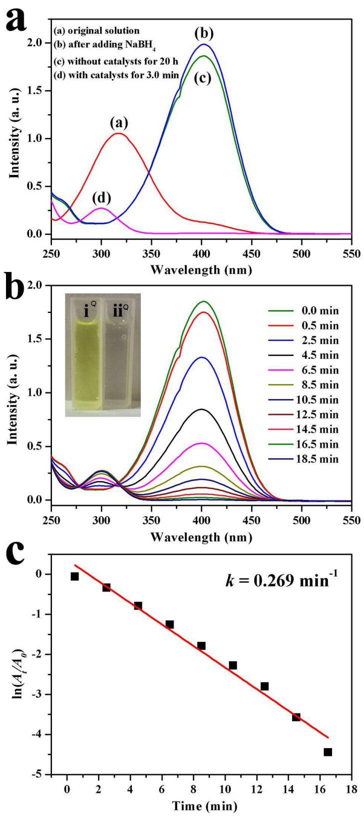

Fig. 8 (a) UV-Vis spectra of the 4-NP solution in different experimental procedure; (b) time-dependent UV-Vis absorption spectra of reduction of 4-NP by $NaBH_4$ in the presence of rGO/$Pd_{48}Au_{52}$/PPy composites; inset shows the digital image of mixture before (i) and after (ii) adding the composites; (c) the rate constant *k* estimated by the slopes of straight lines of ln(A_t/A_0) *vs.* reduction time *t*.

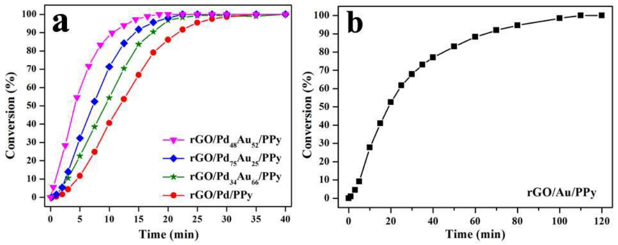

Fig. 9 (a) Conversion of 4-NP using rGO/Pd/PPy, rGO/$Pd_{34}Au_{66}$/PPy, rGO/$Pd_{48}Au_{52}$/PPy and rGO/$Pd_{75}Au_{25}$/PPy composites for various times; (b) conversion of 4-NP using rGO/Au/PPy composites for various times.

Fig. 8b displays the time-dependent UV-Vis absorption spectrum during the reduction reaction in the presence of the as-prepared rGO/$Pd_{48}Au_{52}$/PPy composites. In this study, the dosage of rGO/$Pd_{48}Au_{52}$/PPy composites was reduced to only 3.5 μg. The absorption of the 4-nitrophenolate anions at 400 nm decreases accompanied by a concomitant increase in the 300 nm peak of 4-AP. The bright yellow color of the 4-NP solution is completely bleached within 18.5 min (inset of Fig. 8b), suggesting the completion of the reaction. Based on the evolution of the absorbance data, the reaction rate constant *k* was calculated.[37] A linear relationship of ln(A_t/A_0) *vs.* reaction time *t* is observed in Fig. 8c, which matches well with the pseudo-first-order equation, and the *k* value is calculated to be 0.269 min^{-1} .

The catalytic activities of other catalysts with different molar ratio were also investigated. As shown in Fig. 9a, for rGO/Pd/PPy, rGO/$Pd_{34}Au_{66}$/PPy, and rGO/$Pd_{75}Au_{25}$/PPy composites, the catalytic reactions finish within 40 min, and their reaction rate constant is calculated to be 0.15, 0.18 and 0.23 min^{-1}, respectively. Among all these catalysts, the catalytic activity of rGO/Au/PPy composites is the lowest, and their value is 0.036 min^{-1} (Fig. 9b). Based on these data, it was easily concluded that compared with monometallic nanoparticles, the strong synergistic effect of the Pd_xAu_y bimetallic nanostructures dramatically improved catalytic property.

Conclusion

In summary, we have successfully prepared rGO/Pd_xAu_y/PPy composites with Pd_xAu_y bimetallic nanostructures supported on rGO nanosheet surface and wrapped in PPy layer. The morphologies of Pd_xAu_y nanostructures could be easily turned by simply controlling the molar ratio or dosage of $PdCl_2$ and $HAuCl_4{\cdot}4H_2O$. With increasing of molar ratio of $PdCl_2$ to $HAuCl_4{\cdot}4H_2O$, the bimetallic nanostructures tended to form spherical nanoparticles. When the dosage of $PdCl_2$ and $HAuCl_4{\cdot}4H_2O$ increased, porous nanoclusters appeared on the rGO nanosheet surface. Pyrrole monomer as a special reducing agent played important roles in shaping resulting bimetallic nanostructures. The rGO nanosheets were also an indispensable component in composites. The catalytic activity of rGO/Pd_xAu_y/PPy composites were investigated by reduction of 4-NP with $NaBH_4$ as reducing agent. Compared with monometallic nanoparticles, the Pd_xAu_y bimetallic nanostructures showed improved catalytic property due to synergistic effect.

Acknowledgments

This work was supported by the National Nature Science Foundation of China (Grant no. 51273051, 21174033, 21204015 and 21404035). The Open Project of State Key Laboratory of Supramolecular Structure and Materials (no. sklssm 2015021). The Open Project of Key Laboratory of Functional Inorganic Material Chemistry (Heilongjiang University), Ministry of Education. Natural Science Foundation of Heilongjiang Province of China (E2015005).

Notes and references

1. G. D. Moon, S. W. Choi, X. Cai, W. Y. Li, E. C. Cho, U. Jeong, L. V. Wang and Y. N. Xia, *J. Am. Chem. Soc.*, 2011, **133**, 4762-4765.
2. F. Wang, C. H. Li, L. D. Sun, C. H. Xu, J. F. Wang, J. C. Yu and C. H. Yan, *Angew. Chem., Int. Ed.*, 2012, **51**, 4872-4876.
3. Y. Xu, L. Chen, X. C. Wang, W. T. Yao and Q. Zhang, *Nanoscale*, 2015, **7**, 10559-10583.
4. F. Gao and D. W. Goodmanz, *Chem. Soc. Rev.*, 2012, **41**, 8009-8020.
5. G. H. Wang, J. Hilgert, F. H. Richter, F. Wang, H. J. Bongard, B. Spliethо, C. Weidenthaler and Ferdi Schϋth, *Nat. Mater.*, 2014, **13**, 293-300.
6. H. Y. Liu, L. Y. Zhang, N. Wang and D. S. Su, *Angew. Chem., Int. Ed.*, 2014, **53**, 12634-12638.
7. J. W.i Jiang, S. H. Kim and L. H. Piao, *Nanoscale*, 2015, **7**, 8299-8303.
8. H. Y. Chen, Y. Li, F. B. Zhang, G. L. Zhang and X. B. Fan, *J. Mater. Chem.*, 2011, **21**, 17658-17661.
9. R. Y. Wang, Z. W. Wu, C. M. Chen, Z. F. Qin, H. Q. Zhu, G. F. Wang, H. Wang, C. M. Wu, W. W. Dong, W. B. Fana and J. G. Wang, *Chem. Commun.*, 2013, **49**, 8250-8252.
10. F. H, Li, Y. Q. Guo, R. Q. Li, F. Wu, Y. Liu, X. Y. Sun, C. B. Li, W. Wang and J. P. Gao, *J. Mater. Chem. A*, 2013, **1**, 6579-6587.
11. G. L. Zhang, C. D. Huang, R. J. Qin, Z. C. Shao, D. An, W. Zhang and Y. X. Wang, *J. Mater. Chem. A*, 2015, **3**, 5204-5211.
12. B. Neppolian, C. Wang and M. Ashokkumar, *Ultrason. Sonochem.*, 2014, **21**, 1948-1953.
13. K. Karthikeyan, S. Amaresh, S. N. Lee, J. Y. An and Y. S. Lee, *ChemSusChem*, 2014, **7**, 2310-2316.
14. H. Elzanowska, E. Miasek and V. I. Birsss, *Electrochim. Acta*, 2008, **53**, 2706-2715.
15. M. L. Ma, Q. Y. Zhang, D. Z. Yin, J. B. Dou, H. P. Zhang and H. L. Xu, *Catal.Commun.*, 2012, **17**, 168-172.
16. K. J. Liang, X. Q. Li, S. Z. Kang, L. X. Qin, G. D. Li and J. Mu, *Carbon*, 2014, **80**, 716-724.
17. S. Fujii, A. Aichi, K. Akamatsu, H. Nawafune and Y. Nakamura, *J. Mater. Chem.*, 2007, **17**, 3777-3779.
18. Z. J. Wang, J. H. Yuan, D. X. Han, L. Niu and A. Ivaska, *Nanotechnology*, 2007, **18**, 115610-115614.
19. A. H. Chen, H. Q. Wang and X. Y. Li, *Chem. Commun.*, 2005, 1863-1864.
20. W. S. Hummers and R. E. Offeman, *J. Am. Chem. Soc.*, 1958, **80**, 1339.
21. C. A. Amarnath, C. E. Hong, N. H. Kim, B. C. Ku, T. Kuila and J. H. Lee, *Carbon*, 2011, **49**, 3497-3502.
22. L. Q. Xu, Y. L. Liu, K. G. Neoh, E. T. Kang and G. D. Fu, *Macromol. Rapid Commun.*, 2011, **32**, 684-688.
23. H. Zhou, T. Ni, X. T. Qing, X. X. Yue, G. Li and Y. Lu, *RSC Adv.*, 2014, **4**, 4134-4139.
24. W. Yao, F. L. Li, H. X. Li and J. P. Lang, *J. Mater. Chem. A*, 2015, **3**, 4578-4585.
25. C. H. Liu, R. H. Liu, Q. J. Sun, J. B. Chang, X. Gao, Y. Liu, S. T. Lee, Z. H. Kang, S. D. Wang, *Nanoscale*, 2015, **7**, 6356-6362.
26. W. Qian, R. Hao, J. Zhou, M. Eastman, B. A. Manhat, Q. Sun, A. M. Goforth, J. Jiao, *Carbon*, 2013, **52**, 595-604.
27. X. M. Chen, Z. X. Cai, X. Chen and M. Oyamac, *J. Mater. Chem. A*, 2014, **2**, 5668-5674.
28. N. Lingappan, Y. S. Gal and K. T. Lim, *Mol. Cryst. Liq. Cryst.*, 2013, **585**, 60-66.
29. S. Fujii, S. P. Armes, R. Jeans, R. Devonshire, S. Warren, S. L. McArthur, M. J. Burchell, F. Postberg and R. Srama, *Chem. Mater.*, 2006, **18**, 2758-2765.
30. D. C. Luo, G. X. Zhang, J. F. Liu and X. M. Sun, *J. Phys. Chem. C*, 2011, **115**, 11327-11335.
31. T. J. Yao, Q. Zuo, H. Wang, J. Wu, B. F. Xin, F. Cui and T. Y. Cui, *J. Colloid Interface Sci.*, 2015, **450**, 366-373.
32. S. S. Li, J. J. Lv, Y. Y. Hu, J. N. Zheng, J. R. Chen, A. J. Wang and J. J. Feng, *J. Power Sources*, 2014, **247**, 213-218.
33. L. H. Lu, R. Capek, A. Kornowski, N. Gaponik and A. Eychmuller, *Angew. Chem., Int. Ed.*, 2005, **44**, 5997-6001.
34. K. M. Au, M. Chen, S. P. Armes and N. F. Zheng, *Chem. Commun.*, 2013, **49**, 10525-10527.
35. K. K. Haldar, S. Kundu and A. Patra, *ACS Appl. Mater. Interfaces*, 2014, **6**, 21946-21953.
36. S. Tang, S. Vongehr, X. Meng, *J. Phys. Chem. C*, 2010, **114**, 977-982.
37. E. Lam, S. Hrapovic, E. Majid, J. H. Chong and J. H. T. Luong, *Nanoscale*, 2012, **4**, 997-1002.